Contents lists available at ScienceDirect

Comput. Methods Appl. Mech. Engrg.

journal homepage: www.elsevier.com/locate/cma

A wetting and drying treatment for the Runge–Kutta discontinuous Galerkin solution to the shallow water equations

Shintaro Bunya [a], Ethan J. Kubatko [b], Joannes J. Westerink [c], Clint Dawson [d,*]

[a] The University of Tokyo, 7-3-1 Hongo, Bunkyo, Tokyo 113-8656, Japan
[b] The Ohio State University, Columbus, OH 43210, United States
[c] University of Notre Dame, Notre Dame, IN 46556, United States
[d] The University of Texas at Austin, Austin, TX 78712, United States

ARTICLE INFO

ABSTRACT

This paper proposes a wetting and drying treatment for the piecewise linear Runge–Kutta discontinuous Galerkin approximation to the shallow water equations. The method takes a fixed mesh approach as opposed to mesh adaptation techniques and applies a post-processing operator to ensure the positivity of the mean water depth within each finite element. In addition, special treatments are applied in the numerical flux computation to prevent an instability due to excessive drying. The proposed wetting and drying treatment is verified through comparisons with exact solutions and convergence rates are examined. The obtained orders of convergence are close to or approximately equal to 1 for solutions with discontinuities and are improved for smooth solutions. The combination of the proposed wetting and drying treatment and a TVB slope limiter is also tested and is found to be applicable on condition that they are applied exclusively to an element at the same Runge–Kutta step.

1. Introduction

The shallow water equations (SWE) describe flows for processes such as tides, storm surge, and flows within ocean basins, on shelves, in bays, through inlets, in rivers, and on coastal floodplains. Due to the wide ranges of spatial scales and complex geometries that are present in many applications, unstructured grid methods are an attractive solution strategy. Within the framework of Finite Element (FE) solutions, the standard continuous Galerkin (CG) method has been widely used (e.g. [1–6]) and, more recently, the discontinuous Galerkin (DG) method has been applied [7–16]. The DG method has proven to be very effective in solving the SWE and accurately represents long wave propagation as well as advection processes within a unified framework.

Many problems of interest involve wetting and drying zones which occur, for example, in inter-tidal flats and/or in riverine and coastal floodplains. In the wetting and drying zone, water inundates or recedes as it is driven by tides, wind forces, and/or storm surge. The difficulty in numerically modeling dry areas relates to the obvious fact that there is no water in these areas, i.e. the water column height is zero, and the SWE are only defined for wet regions. This implies that we need to deal with moving boundary problems for the SWE. Moving boundary problems for the shallow water equations are often called wetting and drying problems. In this

paper we present a wetting and drying method devised for the Runge–Kutta discontinuous Galerkin (RKDG) solution to the SWE.

Existing wetting and drying treatments for CG based finite element solutions are categorized into three types [17]. The first type, mesh adaptation techniques, uses a deforming domain and mesh. In this case, the domain and the finite element mesh are deformed as water surface elevations change so that the boundary of the mesh matches the edge of a water body. The mesh adaptation techniques have advantages in accuracy as they can precisely track the location of wetting and drying fronts. However, they tend to be computationally expensive and encounter difficulties in handling complex boundary shapes. As real world problems tend to have intricate topographic contours and boundary shapes, a fixed mesh is more suited to geophysical and engineering problems of interest. Also, it seems that methods based on mesh adaptation techniques do not always yield more accurate solutions than methods using fixed meshes. The second type, mesh reduction techniques, discretely eliminate elements and nodes when the water depth falls below a specified minimum. The eliminated elements and nodes are restored when the water depth rises above a specified maximum. Because mesh reduction techniques involve discrete and sudden elimination of elements/nodes, they may cause oscillations as well as loss of mass and momentum. The last type, thin layer techniques, also uses a fixed mesh. These techniques maintain a thin layer of water in nominally dry elements. In this way, dry elements are conceptually modeled by reducing flow without eliminating elements or nodes. An advantage of the thin layer

---

* Corresponding author.
E-mail address: clint@ices.utexas.edu (C. Dawson).

element approach is that mass can be conserved because elements maintain full connectivity within the continuity or conservation of water volume equation. Furthermore, water in nominally dry elements is kept in these elements until they are restored as fully wet. On the other hand, conservation of momentum is not guaranteed. The thin water layer technique cannot place grid points precisely on shorelines since they use fixed meshes. The exact shoreline may be located in the middle of an element. In such elements, an erroneous gradient is maintained in water surface as part of the bottom may be higher than the height of the exact shorelines and the water surface in such part is artificially lifted above the bottom. This artificial gradient in water surface and the gravity generate ficticious flows. Removing or preventing these unphysical flows without altering physical ones is a difficult task inherent in the thin water layer approach. Momentum conservation is often violated in this process [17,18]. The violation of momentum conservation is only acceptable if the error is verified to be sufficiently small.

DG methods have emerged as an attractive solution to the SWE. The DG method is a FE method in that the formulation is based on a weak weighted residual statement of the governing equations and the solution is locally interpolated with bases of any order within each element. On the other hand, DG methods and the finite volume (FV) methods are similar in that they both end up with the element as a control volume. In fact, both DG and FV solutions can locally conserve quantities in each element. A similar approach to thin layer techniques is commonly used in FV schemes to deal with dry cells. For example, Bradford and Sanders [19] used a tolerance in their two-dimensional FV scheme. In their model, updated velocities are computed in a wet cell only if the water depth is greater than the tolerance.

A few wetting and drying treatments for the DG SWE solutions have been reported. Bokhove [20] used a mesh adaptation technique to track wetting and drying boundaries. As previously mentioned, mesh adaptation techniques are usually more accurate, but also their algorithms tend to be more complex. As we plan to couple the hydrodynamics model with transport and other models, it is desired to keep our algorithm less complex. We, therefore, prefer wetting and drying treatments that use fixed meshes. The work of Ern et al. [21] is the closest to our approach at present. They use a slope modification technique to ensure the positivity of water mass. Their method, however, adds mass when the positivity of mass is violated. The method presented in this article does not violate the positivity of mass without adding mass, taking advantage of the fact that each element is considered as a control volume in the DG spatial discretization.

In this paper, we propose a wetting and drying treatment that uses fixed meshes for DG SWE solutions. Our wetting and drying treatment adopts the thin water layer technique so that it can achieve a good balance between accuracy and computational cost. Our treatment monitors the water depth of each dry/partially wet element and controls it by modifying water surface elevations at the end of each Runge–Kutta time marching stage. This surface elevation modification redistributes the water mass within an element so that a positive water depth is maintained. The sum of mass within an element is unchanged through the modification. This ensures local mass conservation. Also, the surface elevation modification is local in each element, i.e. it is done based on the surface elevation and velocity of the element; it does not use the states of the neighboring elements. This is beneficial in terms of parallel computational efficiency because the locality reduces the communication between subdomains. The proposed treatment also involves special handling of numerical fluxes in order to ensure the positivity of water mass in each element.

This paper is organized as follows. In Section 2, our discretization of the SWE based on the Runge–Kutta Discontinuous Galerkin (RKDG) method is summarized. In Section 3, our new wetting and drying treatment is described in detail. In Section 4, the robustness and accuracy of the proposed method are verified for five different wetting and drying problems, and, in Section 5, conclusions are presented.

2. Governing equations and discontinuous Galerkin method

2.1. Governing equations

The two-dimensional SWE consist of the depth-averaged continuity equation and x and y momentum equations as written here in conservative form:

$$\frac{\partial \zeta}{\partial t} + \frac{\partial}{\partial x}(Hu) + \frac{\partial}{\partial y}(Hv) = 0, \tag{1}$$

$$\frac{\partial}{\partial t}(uH) + \frac{\partial}{\partial x}\left(Hu^2 + \frac{1}{2}g(H^2 - h^2)\right) + \frac{\partial}{\partial y}(Huv) = g\zeta\frac{\partial h}{\partial x}, \tag{2}$$

$$\frac{\partial}{\partial t}(vH) + \frac{\partial}{\partial x}(Huv) + \frac{\partial}{\partial y}\left(Hv^2 + \frac{1}{2}g(H^2 - h^2)\right) = g\zeta\frac{\partial h}{\partial y}, \tag{3}$$

where ζ is the elevation of the free surface measured from a reference level positive upward, h is the bathymetric depth measured from the same reference level, but positive downward, $H = \zeta + h$ is the total height of the water column (water depth), g is the acceleration of gravity, u and v are the depth-averaged velocities in the x and y directions, respectively. Additional forces such as bottom friction, viscous stresses, Coriolis force, tidal potential forces, and wind surface stresses are not considered in this paper.

We define a variable vector as follows:

$$\mathbf{w} \equiv [w_1, w_2, w_3]^T \equiv [\zeta, p, q]^T, \tag{4}$$

where $p \equiv uH$ and $q \equiv vH$. The SWE can then be written in the following divergence form:

$$\frac{\partial w_i}{\partial t} + \nabla \cdot \mathbf{F}_i(\mathbf{w}) = s_i(\mathbf{w}), \quad i \in \{1, 2, 3\}, \tag{5}$$

where $\mathbf{F}_i$ is the ith row of the flux function matrix whose columns are the flux function vectors in the x and y directions denoted by $\mathbf{f}_x$ and $\mathbf{f}_y$, respectively:

$$\mathbf{F} = [\mathbf{f}_x, \mathbf{f}_y] = \begin{bmatrix} uH & vH \\ Hu^2 + \frac{1}{2}g(H^2 - h^2) & Huv \\ Huv & Hv^2 + \frac{1}{2}g(H^2 - h^2) \end{bmatrix}, \tag{6}$$

and finally s_i is the ith component of the vector $\mathbf{s}$ of source/sink terms which is given by:

$$\mathbf{s} = \left[0, g\zeta\frac{\partial h}{\partial x}, g\zeta\frac{\partial h}{\partial y}\right]^T. \tag{7}$$

2.2. Discretization

We first introduce the notation that will be used. Given a domain $\Omega \subset \mathbb{R}^2$, which has been triangulated into a set of non-overlapping, but not necessarily conforming elements, let Ω_K define the domain of an element K and $\partial\Omega_K$ denote the boundary of the element. An inner product taken over Ω_K will be denoted by $(\cdot, \cdot)_{\Omega_K}$, and an inner product taken over $\partial\Omega_K$ will be denoted by $\langle\cdot, \cdot\rangle_{\partial\Omega_K}$. The outward unit normal vector of $\partial\Omega_K$ will be denoted by $\mathbf{n}$.

We approximate $\mathbf{w}$ by $\mathbf{w}_h$, the components of which belong to the space of piecewise smooth functions that are differentiable over an element, but which allow discontinuities between elements. We denote this space of functions by V_h. The SWE are put

into a discrete weak form by replacing $\mathbf{w}$ by $\mathbf{w}_h$, multiplying each equation by a test function $v \in V_h$, integrating over each element, and integrating the divergence term by parts:

$$\left(\frac{\partial}{\partial t}(w_h)_i, v\right)_{\Omega_K} - (\nabla v, \mathbf{F}_i)_{\Omega_K} + \langle \mathbf{F}_i \cdot \mathbf{n}, v \rangle_{\partial\Omega_K} = (s_i, v)_{\Omega_K}, \quad (8)$$

where $(w_h)_i$ is the ith component of $\mathbf{w}_h$. Due to the fact that discontinuities are permitted along $\partial\Omega_K$, the flux $\mathbf{F}$, which may be dual-valued along $\partial\Omega_K$, is replaced in the boundary integral by a single-valued numerical flux denoted by $\widehat{\mathbf{F}}$. Making this substitution the discrete weak formulation of the problem is now given by:

$$\left(\frac{\partial}{\partial t}(w_h)_i, v\right)_{\Omega_K} - (\nabla v, \mathbf{F}_i)_{\Omega_K} + \langle \widehat{\mathbf{F}}_i \cdot \mathbf{n}, v \rangle_{\partial\Omega_K} = (s_i, v)_{\Omega_K}, \quad (9)$$

where $\widehat{\mathbf{F}}_i$ is the ith row of $\widehat{\mathbf{F}}$.

To complete the spatial discretization, we use the local Lax–Friedrich flux to compute the numerical flux $\widehat{\mathbf{F}}$ (see, for example, [22]), Gaussian quadrature to evaluate integrals, and Dubiner's orthogonal triangular basis functions [23]. The second-order Runge–Kutta scheme is used for the time discretization. Cockburn and Shu's slope limiter [22] is applied. Refer to [16,24] for more details on our hydrodynamic model.

3. Wetting and drying treatment

Our wetting and drying treatment is based on the concept of the thin water layer technique, which is explained in Section 1. The most basic requirement to the wetting and drying treatment for this approach is to keep the water column depth greater than zero so that the SWE can have a stable numerical solution over the domain. A wetting (or drying) element is represented by reduced flows; a completely dry element/node is represented by still water of a small depth. To realize this concept, we first propose an operator to keep the water depth within an element positive pointwise for the condition that the mean water depth of the element is positive. The positivity of the mean water depth is ensured by the treatments for numerical flux computation, which will be introduced in Sections 3.3 and 3.4.

In the discussion below, we assume triangular elements and linear approximations of surface elevation ζ and discharges p (=uH) and q (=vH). After each stage of the Runge–Kutta method, the computed surface elevation ζ, and discharges p and q are examined and modified as necessary. As is common in finite element terminology, we refer to the vertices of the triangle as nodes. Let $\overline{H}_K$ denote the average water depth of element K, and ζ_i, H_i, p_i and q_i denote the approximated surface elevation, water depth, discharge in the x-direction, and discharge in the y-direction, at node $i \in \{1, 2, 3\}$, respectively.

3.1. Positive-depth operator

Here, we propose an operator to keep the water depth positive. We name the operator the Positive-Depth (PD) operator and represent it by $M\Pi_h$. The operator $M\Pi_h$ may be used in conjunction with a TVB limiter $\Lambda\Pi_h$ in the k-stage Runge–Kutta time marching algorithm as follows:

- Set $\mathbf{w}_h^0 = \Lambda\Pi_h M\Pi_h P_{V_h}(\mathbf{w}_0)$;
- For $n = 0, \ldots, N-1$ compute $\mathbf{w}_h^{n+1}$ as follows:
  (1) For $i = 1, \ldots, k+1$ compute the intermediate functions:

$$\mathbf{w}_h^{(i)} = \Lambda\Pi_h M\Pi_h \left\{ \sum_{l=0}^{i-1} \alpha_{il} \mathbf{w}_h^{(l)} + \beta_{il} \Delta t L_h(\mathbf{w}_h^{(l)}) \right\}.$$

  (2) set $\mathbf{w}_h^{n+1} = \mathbf{w}_h^{(k+1)}$

where P_{V_h} is a projection to the function space V_h and α_{il} and β_{il} are the constants of the Runge–Kutta method. The purpose of the operator $M\Pi_h$ is to prevent non-positive water depths. To define the operator $M\Pi_h$, we introduce a threshold H_0 to detect nodes that are about to dry.

We construct the operator $M\Pi_h$ on piecewise linear solution functions for the SWE in such a way that the following properties are satisfied:

(1) Accuracy: if $H_h \geq H_0$, $\forall(x,y) \in \Omega_K$,

$$M\Pi_h \mathbf{w}_h = \mathbf{w}_h, \quad \forall(x,y) \in \Omega_K.$$

(2) Conservation of mass: for every element K, we have

$$\int_{\Omega_K} M\Pi_h H_h d\Omega = \int_{\Omega_K} H_h d\Omega.$$

(3) Water surface modification: the slope of water surface is modified in such a way that

$$M\Pi_h H_h \geq H_0, \quad \forall(x,y) \in \Omega_K$$

if this is possible without violating property 3.1. If not possible, then the water depth is set to the mean value over the subdomain $\overline{H}_K$:

$$M\Pi_h H_h = \overline{H}_K, \quad \forall(x,y) \in \Omega_K.$$

(4) Discharge limiting: discharge vanishes at a node if the water depth at the node is less than H_0. The removed discharge is distributed to other nodes to recover the momentum conservation unless the water depth is less than H_0 at all the nodes.

Note that these properties do not prohibit violation of momentum conservation while the second property requires mass conservation. We allowed loss of momentum to ensure that discharge at the wetting and drying front vanishes. To satisfy the properties listed above, it is clear that we have to introduce two different operators: an operator for the water depth, which is denoted by $M\Pi_h^d$, and the other operator for the discharge, which is denoted by $M\Pi_h^f$.

In general, we can write a piecewise linear function u_h with the values at the nodes u_i and the linear basis functions ϕ_i that take a value of 1 at node i and 0 at the other two nodes as follows:

$$u_h(x,y) = \sum_{i=1}^{3} u_i \phi_i(x,y), \quad (x,y) \in \Omega_K.$$

We denote by $\widehat{H}_h$ and $\widehat{H}_i$ the water depth updated by the operator $M\Pi_h^d$ and its nodal values, respectively. Then, we have

$$\widehat{H}_h \equiv M\Pi_h^d H_h = \sum_{i=1}^{3} \widehat{H}_i \phi_i. \quad (10)$$

We now determine $\widehat{H}_i$ to complete the definition of the operator $M\Pi_h^d$:

(1) If $H_i \geq H_0$, $\forall i \in \{1,2,3\}$, then

$$\widehat{H}_i = H_i, \quad \forall i \in \{1,2,3\}. \quad (11)$$

(2) If $\overline{H}_K \leq H_0$, then

$$\widehat{H}_i = \overline{H}_K, \quad \forall i \in \{1,2,3\}. \quad (12)$$

(3) Otherwise, we first find the order of nodal indices $n_i \in \{1,2,3\}$ that satisfies the following inequalities:

$$H_{n_1} \leq H_{n_2} \leq H_{n_3}, \quad (13)$$

then, determine $\widehat{H}_{n_1}$, $\widehat{H}_{n_2}$ and $\widehat{H}_{n_3}$ in the following sequence:

(a) Set $\widehat{H}_{n_1}$:

$$\widehat{H}_{n_1} = H_0. \tag{14}$$

(b) Set $\widehat{H}_{n_2}$:

$$\widehat{H}_{n_2} = \max(H_0, H_{n_2} - (\widehat{H}_{n_1} - H_{n_1})/2). \tag{15}$$

(c) Set $\widehat{H}_{n_3}$:

$$\widehat{H}_{n_3} = H_{n_3} - (\widehat{H}_{n_1} - H_{n_1}) - (\widehat{H}_{n_2} - H_{n_2}). \tag{16}$$

With the operator $M\Pi_h^d$, the water depth in element K is kept the same if the water depth is greater than or equal to H_0 at all the nodes. If the mean water depth is less than or equal to H_0, the updated depth, $\widehat{H}_h$, is set to be $\overline{H}_K$; i.e. the slope of the surface elevation is changed to be parallel to the bottom. Otherwise, the slope of the depth H_h is limited in such a way that $\widehat{H}_h \geqslant H_0$ for all $(x,y) \in \Omega_K$ by redistributing water mass locally in an element. The division by two in Eq. (15) is introduced to lower the depths at nodes n_2 and n_3 by an equal amount. This is more clearly explained by assuming $H_0 < H_{n_2} - (\widehat{H}_{n_1} - H_{n_1})/2$ and substituting Eq. (15) into Eq. (16) to get

$$\widehat{H}_{n_3} = H_{n_3} - (\widehat{H}_{n_1} - H_{n_1})/2. \tag{17}$$

The second property (mass conservation) is always satisfied as Eq. (16) leads to

$$\widehat{H}_{n_1} + \widehat{H}_{n_2} + \widehat{H}_{n_3} = H_{n_1} + H_{n_2} + H_{n_3}. \tag{18}$$

It is clear that the operator $M\Pi_h^d$ satisfies the first, second and third properties.

We next define a discharge operator $M\Pi_h^f$. Discharge in the x-direction p_h can be written with the values at the nodes, p_i as follows:
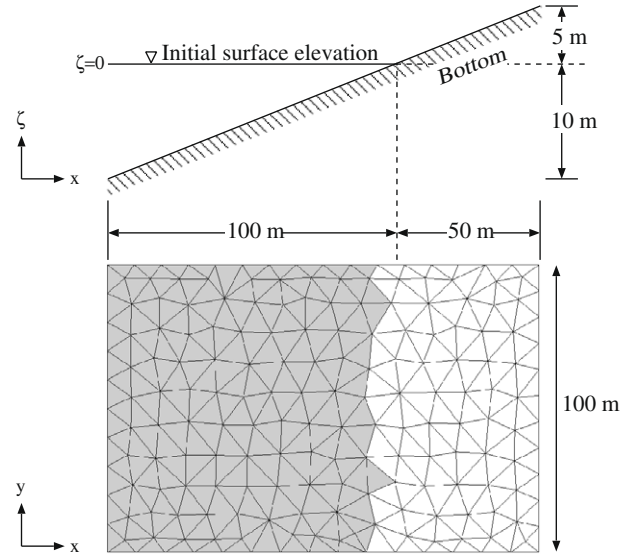
$$p_h = \sum_{i=1}^{3} p_i \phi_i. \tag{19}$$

Fig. 2. Schematic defining the still water problem. Initially wet elements are shadowed in gray.

We define Θ_i, n_{pos} and Δp as follows:

$$\Theta_i = \Theta(\widehat{H}_i - H_0), \tag{20}$$

$$n_{\text{pos}} = \sum_{i=1}^{3} \Theta_i, \tag{21}$$

$$\Delta p = \sum_{i=1}^{3} p_i (1 - \Theta_i), \tag{22}$$

where $\Theta(\cdot)$ is the unit step function defined as

$$\Theta(a) = \begin{cases} 0 & \text{if } a \leqslant 0, \\ 1 & \text{if } a > 0, \end{cases} \tag{23}$$
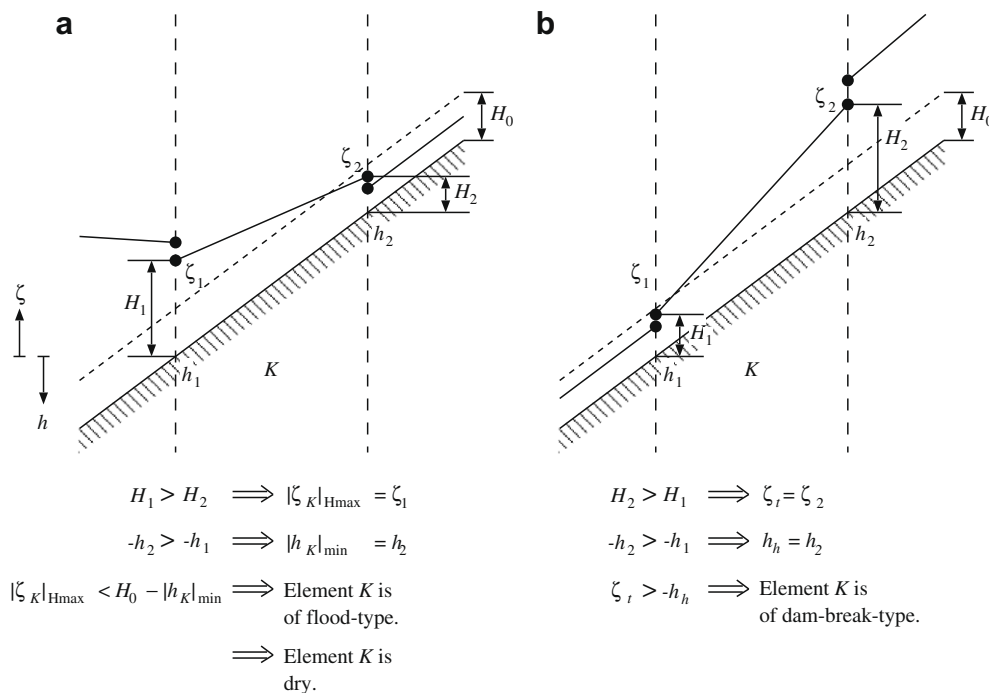

$$H_1 > H_2 \implies |\zeta_K|_{\text{Hmax}} = \zeta_1$$

$$-h_2 > -h_1 \implies |h_K|_{\text{min}} = h_2$$

$$|\zeta_K|_{\text{Hmax}} < H_0 - |h_K|_{\text{min}} \implies \text{Element } K \text{ is of flood-type.}$$

$$\implies \text{Element } K \text{ is dry.}$$

$$H_2 > H_1 \implies \zeta_t = \zeta_2$$

$$-h_2 > -h_1 \implies h_h = h_2$$

$$\zeta_t > -h_h \implies \text{Element } K \text{ is of dam-break-type.}$$

Fig. 1. Examples of the dam break-type and flood-type wetting/drying situations.

Θ_i is the flag that tells whether node i is wet or dry based on the updated water depth, n_{pos} is the number of wet nodes and Δp is the sum of discharge in the x-direction at the dry nodes.

The operator $M\Pi_h^f$ is now defined as follows:

$$\hat{p}_h \equiv M\Pi_h^f p_h = \sum_{i=1}^{3} \hat{p}_i \phi_i, \tag{24}$$

where

$$\hat{p}_i = \Theta_i \cdot (p_i + \Delta p / n_{pos}). \tag{25}$$

Eq. (25) distributes the momentum removed at dry nodes to wet nodes. The operator $M\Pi_h^f$ satisfies the first and fourth properties. It violates the momentum conservation only when $\hat{H}_i \leqslant H_0$ for all $i \in \{1, 2, 3\}$.

The discharge in the y-direction, q_h, is limited by the same operator $M\Pi_h^f$:

$$\hat{q}_h \equiv M\Pi_h^f q_h. \tag{26}$$

3.2. TVB slope limiter

In RKDG methods, a slope limiter may need to be applied to remove high-frequency oscillations to avoid instability. Thus we use Cockburn and Shu's TVB limiter [22]. The details of their slope limiter are not repeated here. We write only the definition of the modified minmod function as the parameter M will appear when we solve test problems with the slope limiter. Note that the choice of M is problem-dependent. The modified minmod function, $\bar{m}(\cdot)$, is defined as follows:

$$\bar{m}(a_1, \ldots, a_m) = \begin{cases} a_1 & \text{if } |a_1| \leqslant M\Delta x^2, \\ m(a_1, \ldots, a_m), & \text{otherwise,} \end{cases} \tag{27}$$

where $m(\cdot)$ is the minmod function and a_i's are arbitrary numbers.

As reported in [21], a wetting and drying treatment and a slope limiter may artificially activate each other. This conflicts may cause an instability. Therefore, the slope limiter is applied only when the wetting and drying treatment is not applied at the same RK step.

3.3. A stability condition for the thin water layer approach

The goal of this section is to provide a sufficient condition to ensure the positivity of mean water depth in each element. We begin by considering the balance between the existing mass in an element and the outgoing discharge through its boundary. The balance is, in fact, written as the mass conservation equation as in Eq. (9) for $i = 1$. We write it here again with some rearrangements:

$$\left(\frac{\partial H_h}{\partial t}, 1 \right)_{\Omega_K} = -\langle \widehat{\mathbf{F}}_1 \cdot \mathbf{n}, 1 \rangle_{\partial \Omega_K}, \tag{28}$$

where test function v is replaced with 1 as we are now interested in the total water mass in the element and net mass exchange between neighboring elements. Since we assume that our element is triangular and the interpolation is linear, Eq. (28) can be further rewritten with the mean water depth $\overline{H}_K$ as follows:

$$\frac{d}{dt}(\overline{H}_K A_K) = -\langle \widehat{\mathbf{F}}_1 \cdot \mathbf{n}, 1 \rangle_{\partial \Omega_K} \tag{29}$$

where A_K is the area of element K. Eq. (29) is then discretized in time using the s-stage Runge–Kutta method as follows:

$$\begin{aligned} \overline{M}_K^{(i)} &\equiv \overline{H}_K^{(i)} A_K = \sum_{l=0}^{i-1} \{ \alpha_{il} \overline{H}_K^{(l)} A_K - \Delta t \beta_{il} \langle \widehat{\mathbf{F}}_1^{(l)} \cdot \mathbf{n}, 1 \rangle_{\partial \Omega_K} \} \\ &= \sum_{l=0}^{i-1} \left\{ \alpha_{il} \left(\overline{H}_K^{(l)} A_K - \Delta t \frac{\beta_{il}}{\alpha_{il}} \langle \widehat{\mathbf{F}}_1^{(l)} \cdot \mathbf{n}, 1 \rangle_{\partial \Omega_K} \right) \right\}, \\ &\quad \alpha_{il} \geqslant 0, \quad i = 1, \ldots, s \end{aligned} \tag{30}$$

where superscript (l) indicates quantities in the lth Runge–Kutta stage. The sufficient condition to ensure the positivity of the mean water depth of element K is

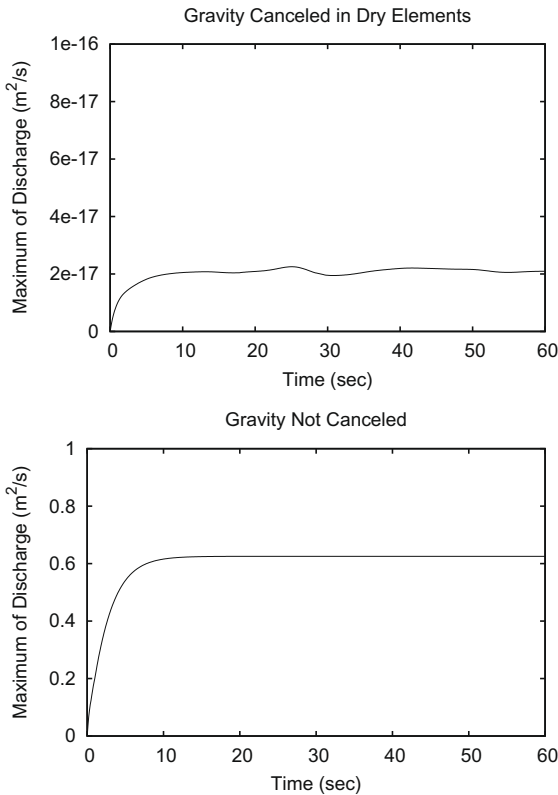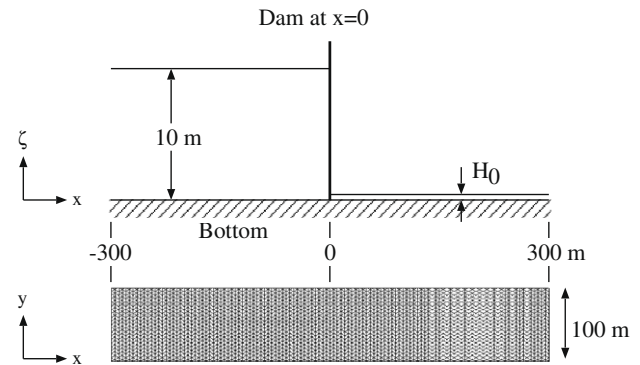$$\overline{M}_K^{(i)} > 0, \quad \forall i \in \{1, \ldots, s\}. \tag{31}$$

Fig. 3. Time history of the maximum magnitude of the discharge over the entire computational domain. Top: the gravity terms are canceled, bottom: the gravity terms are not canceled.

Fig. 4. Schematic defining the dam break problem. The Δx of the computational mesh shown above is 5 m.

Table 1
Model parameters for the dam break problem and drying Riemann problem.

Case ID	Slope limiter	M	H_0 (m)
D1	Not applied	–	10^{-5}
D2	Applied	1	10^{-5}
D3	Applied	0.1	10^{-5}

We define $\overline{M}_{K,l}^{(i)}$ as

$$\overline{M}_{K,l}^{(i)} \equiv \overline{H}_K^{(l)} A_K - \Delta t \frac{\beta_{il}}{\alpha_{il}} \langle \widehat{\mathbf{F}}_1^{(l)} \cdot \mathbf{n}, 1 \rangle_{\partial \Omega_K}. \tag{32}$$

Eqs. (30) and (32) lead to

$$\overline{M}_K^{(i)} = \sum_{l=0}^{i-1} \alpha_{il} \overline{M}_{K,l}^{(i)}. \tag{33}$$

Since $\sum_{l=0}^{i-1} \alpha_{il} = 1$ and $\alpha_{il} \geqslant 0$, $\forall i$, for a general Runge–Kutta method, $\overline{M}_K^{(i)}$ is a convex combination of $\overline{M}_{K,l}^{(i)}$. Also, the combinations of (i,l) where $\alpha_{il} = 0$ can be ignored as $\beta_{il} = 0$ if $\alpha_{il} = 0$ [25]. Therefore, Eq. (31) is satisfied sufficiently if

$$\overline{M}_{K,l}^{(i)} > 0, \quad \forall l \in \{0, \ldots, i-1 | \alpha_{il} \neq 0\}. \tag{34}$$

Eqs. (32) and (34) give the following restriction on Δt to satisfy Eq. (31) sufficiently:

$$\Delta t < \frac{\alpha_{il}}{\beta_{il}} \frac{\overline{H}_K^{(l)} A_K}{\langle \widehat{\mathbf{F}}_1^{(l)} \cdot \mathbf{n}, 1 \rangle_{\partial \Omega_K}} \quad \text{if } \langle \widehat{\mathbf{F}}_1^{(l)} \cdot \mathbf{n}, 1 \rangle_{\partial \Omega_K} > 0,$$

$$\forall l \in \{0, \ldots, i-1 | \alpha_{il} \neq 0\}. \tag{35}$$

Eq. (31) is satisfied with any Δt if $\langle \widehat{\mathbf{F}}_1^{(l)} \cdot \mathbf{n}, 1 \rangle_{\partial \Omega_K} \leqslant 0$. We choose non-negative β_{il} for the sake of efficiency and our choices of α_{il} presented in [24] are also non-negative. Thus, if the mean water depths of previous Runge–Kutta stages, $\overline{H}_K^{(l)}$, are positive, then the right hand side of Eq. (35) is positive. Therefore one can always find a positive Δt that ensures the positivity of mass integrated over an element; i.e. $\overline{M}_K^{(i)} > 0$. Furthermore, once the positivity of the mean water depth is ensured, the PD operator will ensure the pointwise positivity of water depth by the water surface modification.

One can set a sufficiently small Δt to satisfy Eq. (35). However, it is not easy to estimate the right hand side of Eq. (35). It is rather more practical to consider the condition of Eq. (35) in a wetting and drying treatment so that the positivity of the mean water depth is satisfied with any given Δt. Therefore, we consider manipulating the numerical fluxes between neighboring elements in such a way that mass exchange is prohibited once the violation of Eq. (35) is detected. To detect this violation, the flux $\widehat{\mathbf{F}}_1^{(l)}$ must be computed once, and if the violation is detected with the computed flux, then a new flux must be recomputed so that it satisfies $\widehat{\mathbf{F}}_1^{(l)} \cdot \mathbf{n} = 0$.

We compute the numerical flux that prohibits mass transfer in the form of the reflection flux. The reflection flux is computed by an approximated Riemann solver with $\mathbf{w}_{in} \equiv (\zeta_{in}, p_{in}, q_{in})$ and $\mathbf{w}_{in}^{ref} \equiv (\zeta_{in}^{ref}, p_{in}^{ref}, q_{in}^{ref})$. The symbol $\mathbf{w}_{in}$ is the vector of variables on the elemental boundary from the interior of the element. The symbol $\mathbf{w}_{in}^{ref}$ represents the reflected variable vector defined as follows:

$$\zeta_{in}^{ref} = \zeta_{in}, \tag{36}$$

$$\begin{Bmatrix} p_{in}^{ref} \\ q_{in}^{ref} \end{Bmatrix} \cdot \mathbf{n} = - \begin{Bmatrix} p_{in} \\ q_{in} \end{Bmatrix} \cdot \mathbf{n}, \tag{37}$$

$$\begin{Bmatrix} p_{in}^{ref} \\ q_{in}^{ref} \end{Bmatrix} \cdot \mathbf{t} = \begin{Bmatrix} p_{in} \\ q_{in} \end{Bmatrix} \cdot \mathbf{t}, \tag{38}$$

where $\mathbf{t}$ is the unit tangential vector to the elemental boundary $\partial \Omega_K$. The reflection numerical flux can be written as follows:

$$\widehat{\mathbf{F}} = \widehat{\mathbf{F}}(\mathbf{w}_{in}, \mathbf{w}_{in}^{ref}). \tag{39}$$

Table 2
L^2 error norms and convergence rates of the dam break problem: Case D1.

Δx	$L^2(\zeta)$	Rate	$L^2(p)$	Rate	$L^2(q)$	Rate
20.00	6.22E−04	–	6.91E−03	–	1.79E−04	–
10.00	3.19E−04	0.97	3.63E−03	0.93	6.03E−05	1.57
5.00	1.59E−04	1.00	1.79E−03	1.02	2.04E−05	1.56
2.50	7.96E−05	1.00	8.74E−04	1.04	7.26E−06	1.49
1.25	4.01E−05	0.99	4.33E−04	1.02	2.64E−06	1.46
Fitted	–	0.99	–	1.00	–	1.52

Table 3
L^2 error norms and convergence rates of the dam break problem: Case D2.

Δx	$L^2(\zeta)$	Rate	$L^2(p)$	Rate	$L^2(q)$	Rate
20.00	6.31E−04	–	6.98E−03	–	3.04E−04	–
10.00	3.25E−04	0.96	3.68E−03	0.92	6.72E−05	0.22
5.00	1.81E−04	0.85	2.04E−03	0.85	7.16E−05	−0.09
2.50	1.01E−04	0.83	1.16E−03	0.82	1.73E−05	2.05
1.25	5.44E−05	0.90	6.17E−04	0.91	8.34E−06	1.05
Fitted	–	0.88	–	0.87	–	1.23

Table 4
L^2 error norms and convergence rates of the dam break problem: Case D3.

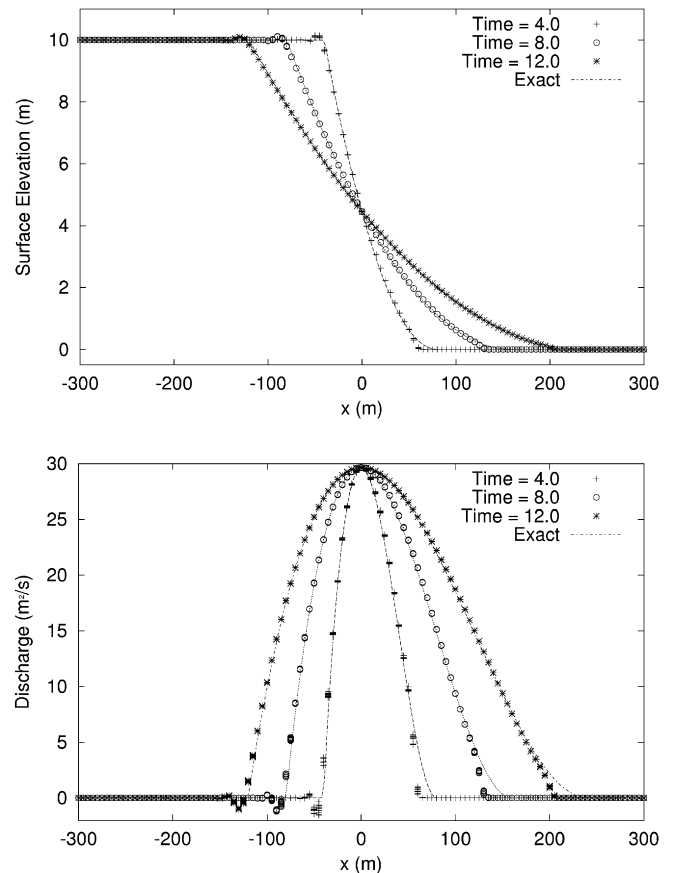| Δx	$L^2(\zeta)$	Rate	$L^2(p)$	Rate	$L^2(q)$	Rate
20.00	6.53E−04	–	7.15E−03	–	3.39E−04	–
10.00	3.55E−04	0.88	3.83E−03	0.90	1.56E−04	1.12
5.00	1.93E−04	0.88	2.05E−03	0.90	5.86E−05	1.41
2.50	1.03E−04	0.90	1.10E−03	0.90	2.27E−05	1.37
1.25	5.48E−05	0.92	5.89E−04	0.90	7.97E−06	1.51
Fitted	–	0.89	–	0.90	–	1.36

Fig. 5. The computed solutions of the dam break problem: Case D1.

The violation of Eq. (35) is detected on each edge of a triangular element and the reflection numerical flux is used only on those edges.

3.4. Flux between dry elements

Besides the flux modification, to ensure the positivity of the water depth, flux between dry elements is also modified to prohibit water mass exchange between neighboring dry elements. The reasons why the mass/momentum exchange needs to be restricted are threefold; (1) to prevent unphysical oscillations from propagating to dry regions, (2) to prevent dry elements from losing all their mass, and (3) to save computation time. The third reason may need some explanation. As long as neighboring elements are coupled through a numerical flux, all the elements including dry elements must be considered in the computation. We can decouple neighboring dry elements by evaluating the flux between dry elements as the reflection flux. After decoupling neighboring dry elements, all the wet elements and only the dry elements neighboring a wet element should be considered in the computation. The rest of the dry elements can be neglected to save computational time. In our present code, this idea to save computational time has not been implemented and both wet and dry elements are considered in computation.

Here we define the wet-or-dry status of element K. Let $\omega_K^{(l)}$ denote the wet-or-dry status; i.e. $\omega_K^{(l)} = 0$ if element K is dry at the lth Runge–Kutta stage and $\omega_K^{(l)} = 1$ otherwise. The wet-or-dry status is determined as follows:

$$\omega_K^{(i)} = \omega_K^{(i-1)}\Theta(\overline{H}_K - H_0) + (1 - \omega_K^{(i-1)})\Theta(\overline{H}_K - H_0)\Theta(|\zeta_K|_{Hmax}$$
$$ - (H_0 - |h_K|_{min})), \tag{40}$$
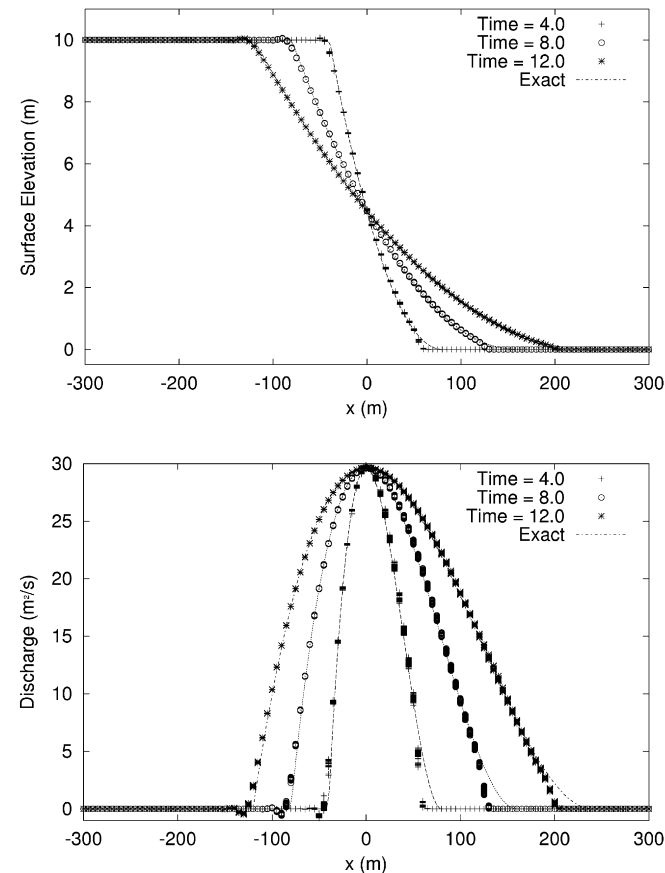
where $|\zeta_K|_{Hmax}$ is the surface elevation at a point where the water depth is the greatest over Ω_K. The symbol $|h_K|_{min}$ represents the
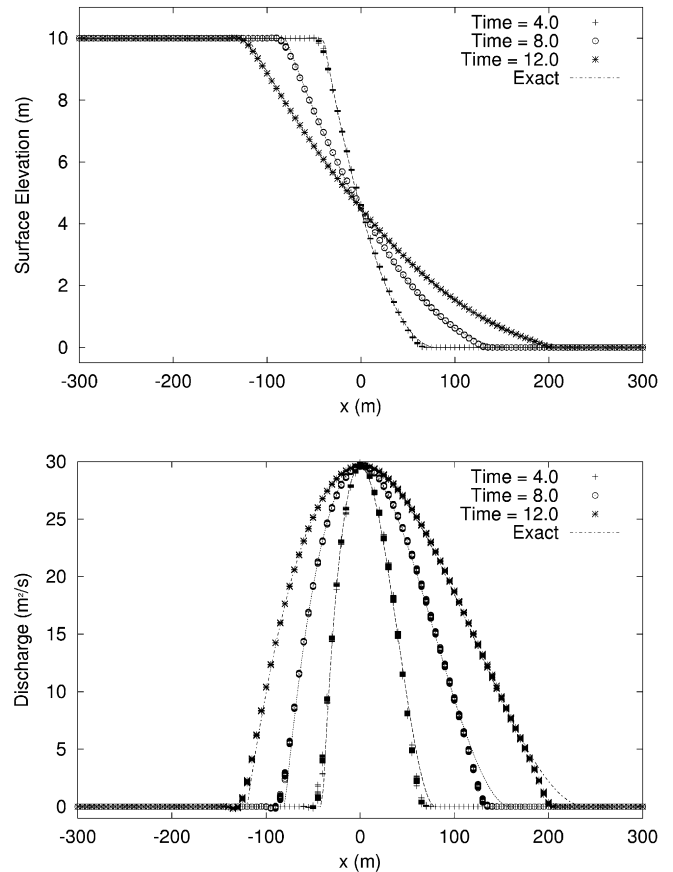

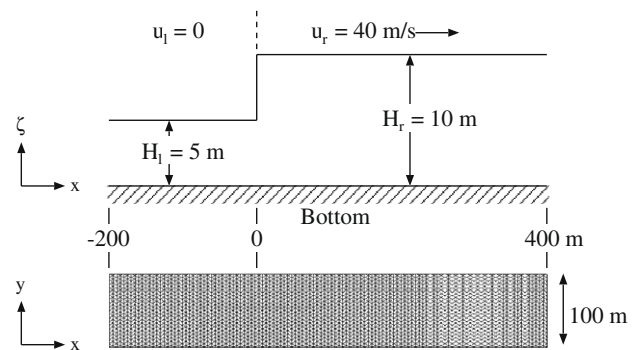Fig. 7. The computed solutions of the dam break problem: Case D3.

Fig. 8. Schematic defining the drying Riemann problem. The Δx of the computational mesh shown above is 5 m.

Fig. 6. The computed solutions of the dam break problem: Case D2.

Table 5
L^2 error norms and convergence rates of the drying Riemann problem: Case D1.

Δx	$L^2(\zeta)$	Rate	$L^2(p)$	Rate	$L^2(q)$	Rate
20.00	1.53E−03	–	0.06	–	3.96E−04	–
10.00	6.75E−04	1.18	2.62E−02	1.20	8.67E−05	2.19
5.00	3.31E−04	1.03	1.31E−02	1.01	2.82E−05	1.62
2.50	1.72E−04	0.95	6.93E−03	0.91	9.95E−06	1.50
1.25	9.00E−05	0.94	3.70E−03	0.91	3.59E−06	1.47
Fitted	–	1.01	–	1.00	–	1.67

highest bottom depth over Ω_K. Note that the positive direction of the bottom depth is vertical downward. This wet-or-dry judgment is partially based on Bates and Hervouet's classification of dam-break-type and flood-type wetting/drying elements [18]. Examples of the dam-break-type and flood-type wetting/drying situations are depicted in Fig. 1.

Table 6
L^2 error norms and convergence rates of the drying Riemann problem: Case D2.

Δx	$L^2(\zeta)$	Rate	$L^2(p)$	Rate	$L^2(q)$	Rate
20.00	1.53E−03	–	6.05E−02	–	6.66E−04	–
10.00	6.83E−04	1.17	2.67E−02	1.18	3.08E−04	1.11
5.00	3.57E−04	0.94	1.40E−02	0.93	2.09E−04	0.56
2.50	1.98E−04	0.85	7.72E−03	0.86	1.36E−04	0.61
1.25	1.06E−04	0.90	4.14E−03	0.90	7.07E−05	0.95
Fitted	–	0.95	–	0.95	–	0.77

Table 7
L^2 error norms and convergence rates of the drying Riemann problem: Case D3.

Δx	$L^2(\zeta)$	Rate	$L^2(p)$	Rate	$L^2(q)$	Rate
20.00	1.50E−03	–	6.12E−02	–	1.05E−03	–
10.00	7.04E−04	1.09	2.76E−02	1.15	9.32E−04	0.18
5.00	3.57E−04	0.98	1.37E−02	1.01	3.80E−04	1.30
2.50	1.93E−04	0.89	7.36E−03	0.90	1.60E−04	1.24
1.25	1.05E−04	0.88	3.98E−03	0.891	6.37E−05	1.33
Fitted	–	0.95	–	0.98	–	1.06

To prevent mass/momentum exchange between dry elements, we compute the reflection flux defined in Section 3.3 and use it as a numerical flux along the inter-element boundary that is sandwiched by dry elements. Thus, with this reflection flux, interaction between neighboring dry elements no longer exists.

3.5. Cancellation of gravity terms

While an element is wetting or drying, till it gets fully wet or dry, an artificial gradient in surface elevation may be observed as the slope is limited by the slope of the bottom. This artificial slope of surface elevation induces unphysical gravitational force according to the gravity terms in the momentum equations. Thus we cancel the gravity terms in dry elements, in which $\omega_K^{(l)} = 0$.

In our formulation presented in Eq. (9), the acceleration of gravity, g, appears in $\mathbf{F}_i$, $\widehat{\mathbf{F}}_i$ and s_i. In evaluating the domain integration terms that contain $\mathbf{F}_i$ and s_i, we simply set $g = 0$ if element K is dry (i.e. $\omega_K^{(l)} = 0$). On the other hand, in obtaining a single-valued numerical flux $\widehat{\mathbf{F}}_i$, it is incorrect to set $g = 0$ since it will violate the balance between the boundary integration terms and domain integration terms. In a wet element neighboring a dry element, in evaluating the domain integration terms, which contains $\mathbf{F}_i$ and s_i, g will be set to a prescribed non-zero value.

To achieve consistent evaluations of $\widehat{\mathbf{F}}_i$ with that of $\mathbf{F}_i$ and s_i, we allow dual-valued numerical fluxes on such inter-element boundaries that are sandwiched by wet and dry elements. One of the numerical flux vectors is computed in the standard way with a prescribed non-zero g. This standard numerical flux is used to evaluate the boundary integrals of wet elements. The other flux is the one for dry elements. We compute it with the same Riemann solver, but with $g = 0$. Denoting the numerical flux computed with $g = 0$
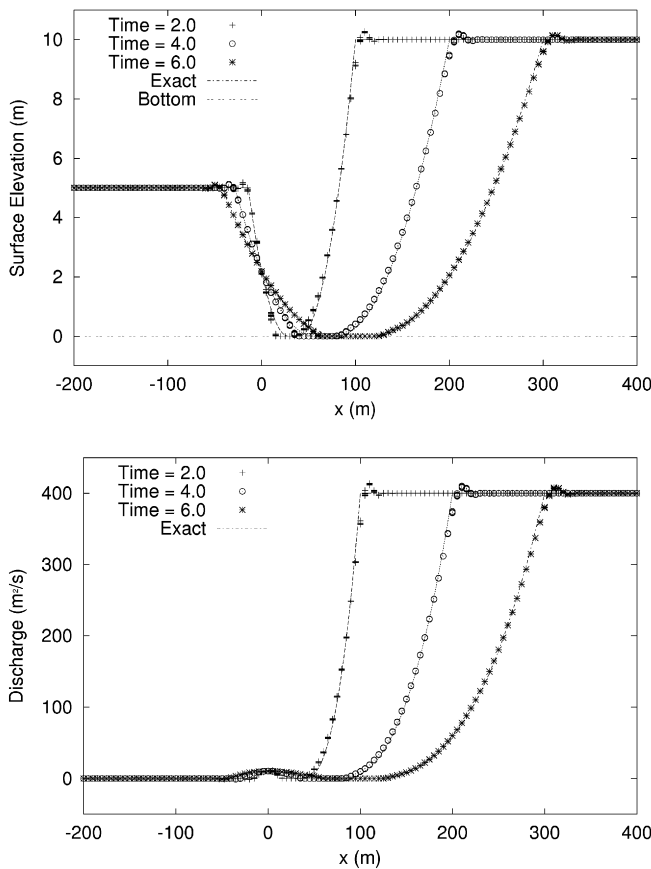

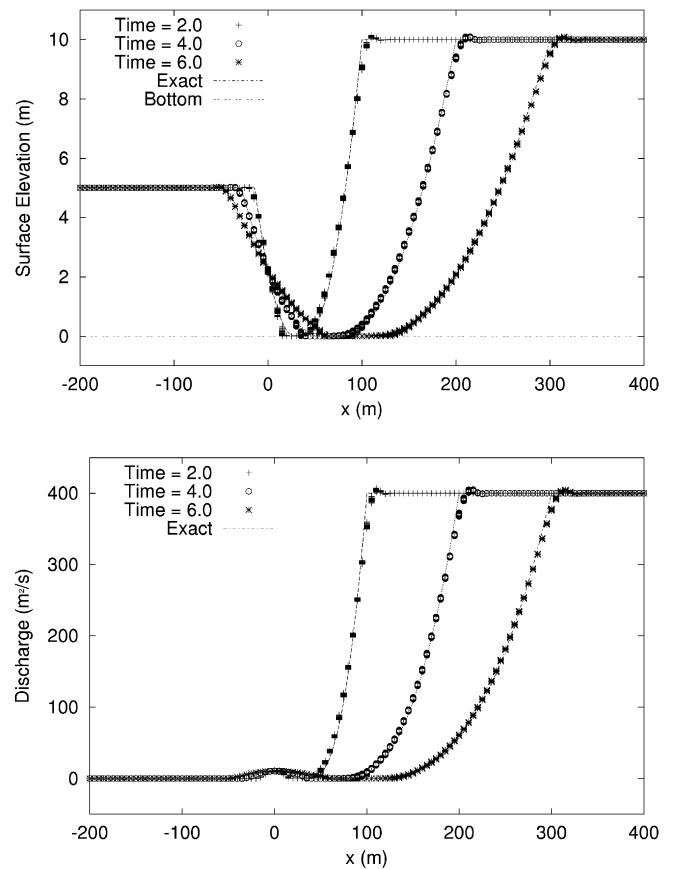Fig. 9. The computed solutions of the drying Riemann: Case D1.

Fig. 10. The computed solutions of the drying Riemann: Case D2.

by $\widehat{\mathbf{F}}_i^d$, the numerical flux is redefined on the inter-element boundary of wet and dry elements as follows:

$$\widehat{\mathbf{F}} = \begin{bmatrix} \widehat{\mathbf{F}}_1 \\ \widehat{\mathbf{F}}_2 \\ \widehat{\mathbf{F}}_3 \end{bmatrix} \text{ on the wet side,}$$

$$\widehat{\mathbf{F}} = \begin{bmatrix} \widehat{\mathbf{F}}_1 \\ \widehat{\mathbf{F}}_2^d \\ \widehat{\mathbf{F}}_3^d \end{bmatrix} \text{ on the dry side.}$$
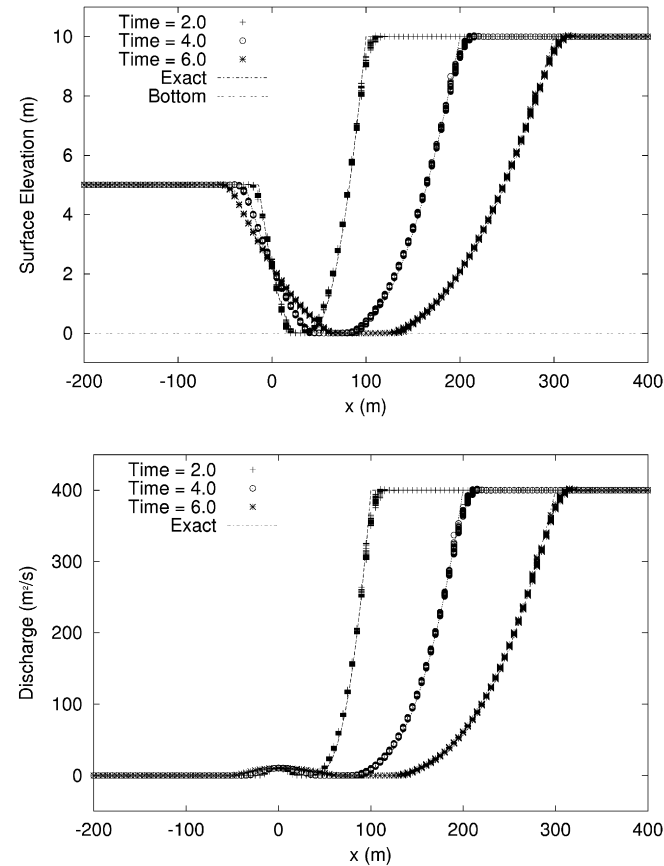

Fig. 11. The computed solutions of the drying Riemann: Case D3.

Fig. 12. Schematic defining the Carrier–Greenspan problem. The Δx of the computational mesh shown above is 0.025 m.

Note that, only on the dry side, the momentum fluxes are replaced with those computed with $g = 0$. Thus we violate the momentum conservation to cancel the gravity terms. On the other hand, the same mass flux is used on both sides. Therefore, mass conservation is intact.

4. Numerical tests

In this section, we verify the wetting and drying method proposed in the previous section. We consider still water at rest, the dam break problem, the drying Riemann problem over a flat bottom, the Carrier–Greenspan solution and a parabolic bowl problem. Convergence studies are conducted for the last four problems. The influence of slope limiting is investigated in some of the test problems. The influence of the threshold H_0 is examined for the Carrier–Greenspan problem. The behavior of the wetting and drying method in a two-dimensional problem is tested in the parabolic bowl problem.

Convergence rates are computed by measuring the following L^2 error norm:

$$L^2(w) = \frac{1}{A}\left[\int_{\Omega}(w_h - w)^2 d\Omega\right]^{\frac{1}{2}}, \tag{41}$$

where Ω is the entire computational domain, A is the area of the domain Ω, w_h is the numerical solution of ζ, p or q, and w is the exact solution.

4.1. Still water at rest

We test our wetting and drying treatment with respect to whether it can produce still water at rest. The problem definition and the finite element mesh are depicted in Fig. 2. The slip boundary condition with no normal flow is applied to the entire boundary. The Courant number is set to 0.1. The surface elevation is initially set to 0 on the nodes where the bottom is below the datum level. The surface elevation on the other nodes are set to 10^{-5} m above the bottom elevation. The initial discharges are set to zero. Thus the water body is initially at rest.

In Fig. 2, initially wet elements are shadowed in gray. The water front is not straight since the mesh is unstructured. The wet-or-dry judgment introduced in Eq. (40) tends to estimate a smaller wet region. This is a desirable property as one should avoid inducing a fictitious flow generated by an artificial gradient in water surface
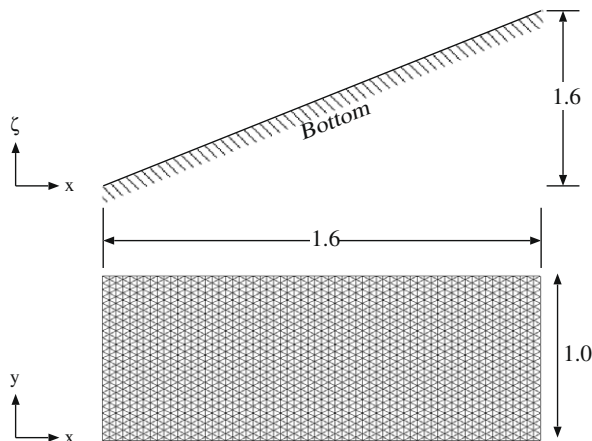
Table 8
Model parameters for the Carrier–Greenspan problem.

Case ID	Slope limiter	M	H_0
CG1	Not applied	–	10^{-5}
CG2	Applied	10	10^{-5}
CG3	Applied	1	10^{-5}
CG4	Not applied	–	10^{-4}
CG5	Not applied	–	10^{-3}

Table 9
L^2 error norms and convergence rates of the Carrier–Greenspan solution: Case CG1.

Δx	$L^2(\zeta)$	Rate	$L^2(p)$	Rate	$L^2(q)$	Rate
0.10000	8.50E−03	–	5.30E−03	–	2.14E−04	–
0.05000	5.58E−03	0.61	1.42E−03	1.90	7.70E−05	1.48
0.02500	2.65E−03	1.07	7.11E−04	1.00	2.55E−05	1.59
0.01250	9.56E−04	1.47	2.57E−04	1.47	6.82E−06	1.90
0.00625	4.67E−04	1.03	1.17E−04	1.14	2.65E−06	1.37
Fitted	–	1.09	–	1.35	–	1.62

near a water front. It approaches the actual water front as mesh resolution is increased.

Fig. 3 shows the time histories of maximum of the magnitude of discharges over the entire computational domain. In this figure, the effect of the gravity cancellation, which was introduced in Section 3.5 is examined. The upper part of the figure is produced from the solution computed with the gravity cancellation. The lower part of the figure is the case without the gravity cancellation. From the upper figure, it is observed that the water body practically stays still if the gravity terms are canceled. From the comparison of the upper and lower figures, it is clear that the gravity cancellation removes the fictitious gravity force. The maximum magnitude of discharges did not grow over the level shown in Fig. 3 in longer simulations for either case.

4.2. Dam break on a dry bed

In this section, we solve the one-dimensional dam break problem on a dry bed using a 2D mesh. The numerical solution is compared with the analytical solution provided in [26]. Fig. 4 shows the computational domain, the initial condition, and one of the computational meshes used in the convergence study presented later. The left side of the dam located at $x = 0$ is initially wet and has still water with the depth of 10 m. The right side of the dam is an initially dry region where the initial water depth is set to H_0. The parameter H_0 is set to 10^{-5} m in this test problem. The acceleration of gravity is 10 m/s^2. The Courant number is 0.1. Lateral slip and no normal flow boundary conditions are applied to all boundaries.

The convergence study is conducted with three sets of parameters shown in Table 1. In Case D1, the slope limiter is not applied. In Cases D2 and D3, the slope limiter is applied with different values of the TVB parameter M for a sensitivity check. The L^2 error norms of Cases D1, D2 and D3 are shown in Tables 2–4, respectively. The rows of the tables labeled as "Fitted" are least square fits of the data. The L^2 error norms are computed with the solutions at $t = 8s$. The convergence rates of the non-slope limiting case (D1) are close to or equal to 1 for ζ and p, and approximately 1.5 for q. The convergence rates close to 1 are satisfactory as one cannot expect a convergence rate greater than 1 if the solution contains a discontinuity. The dam break problem contains a discontinuity in the initial condition. The convergence rate of $L^2(q)$ is considerably greater than 1. This is because the solution is smooth in the y-direction.

The convergence rates degrade when the slope limiter is applied. The combination of the PD operator and TVB limiter does seem to decrease the order of convergence to less than 1, but it is within an acceptable range. Shown in Figs. 5–7 are the exact solutions and the numerical solutions computed with $\Delta x = 5$ m for each of the three cases D1, D2 and D3. The horizontal axis corresponds to the horizontal variable x. The values of the solutions at vertices (x, y) for each y are plotted on the vertical axis. Note that

Table 10
L^2 error norms and convergence rates of the Carrier–Greenspan solution: Case CG2.

Δx	$L^2(\zeta)$	Rate	$L^2(p)$	Rate	$L^2(q)$	Rate
0.10000	1.07E−02	–	5.22E−03	–	3.89E−04	–
0.05000	5.42E−03	0.98	1.51E−03	1.79	7.96E−05	2.29
0.02500	2.65E−03	1.03	7.14E−04	1.08	3.17E−05	1.33
0.01250	9.67E−04	1.46	2.51E−04	1.51	1.08E−05	1.56
0.00625	4.76E−04	1.02	1.03E−04	1.28	3.75E−06	1.52
Fitted	–	1.15	–	1.39	–	1.63

Table 11
L^2 error norms and convergence rates of the Carrier–Greenspan solution: Case CG3.

Δx	$L^2(\zeta)$	Rate	$L^2(p)$	Rate	$L^2(q)$	Rate
0.10000	9.54E−03	–	5.63E−03	–	3.03E−04	–
0.05000	5.56E−03	0.78	1.58E−03	1.83	1.20E−04	1.33
0.02500	2.70E−03	1.04	7.13E−04	1.15	3.68E−05	1.71
0.01250	9.65E−04	1.48	2.49E−04	1.51	1.17E−05	1.65
0.00625	4.75E−04	1.02	1.01E−04	1.30	3.07E−06	1.93
Fitted	–	1.12	–	1.43	–	1.66

Table 12
L^2 error norms and convergence rates of the Carrier–Greenspan solution: Case CG4.

Δx	$L^2(\zeta)$	Rate	$L^2(p)$	Rate	$L^2(q)$	Rate
0.10000	8.61E−03	–	5.12E−03	–	3.27E−04	–
0.05000	5.00E−03	0.78	1.84E−03	1.48	1.24E−04	1.40
0.02500	2.67E−03	0.90	7.40E−04	1.32	4.53E−05	1.45
0.01250	1.04E−03	1.36	2.69E−04	1.46	5.87E−06	2.95
0.00625	5.45E−04	0.93	1.27E−04	1.09	2.17E−06	1.44
Fitted	–	1.02	–	1.34	–	1.89

Table 13
L^2 error norms and convergence rates of the Carrier–Greenspan solution: Case CG5.

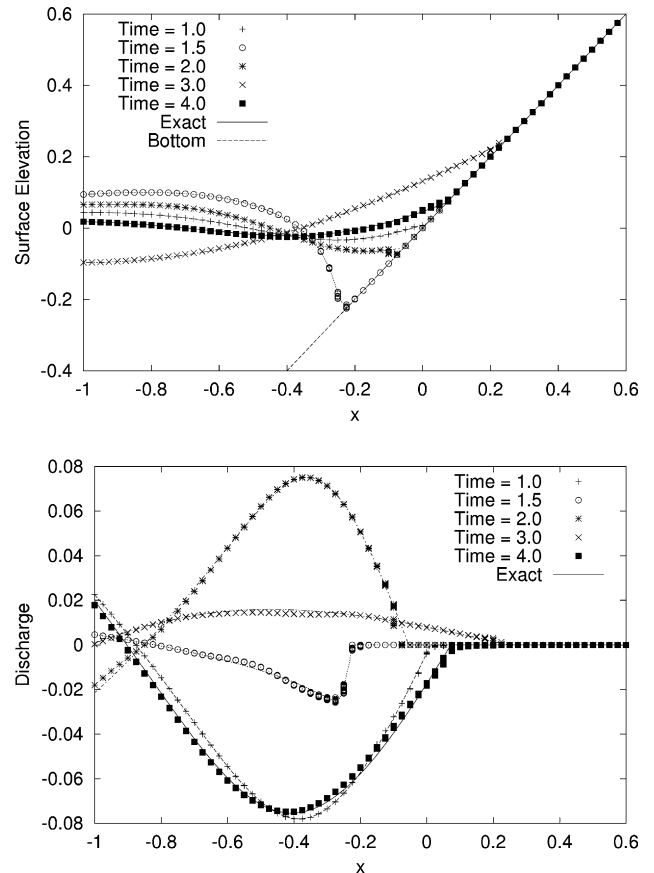| Δx	$L^2(\zeta)$	Rate	$L^2(p)$	Rate	$L^2(q)$	Rate
0.10000	1.42E−02	–	4.68E−03	–	1.15E−04	–
0.05000	6.23E−03	1.19	1.92E−03	1.28	7.85E−05	0.55
0.02500	3.36E−03	0.89	8.06E−04	1.25	1.32E−05	2.57
0.01250	2.31E−03	0.54	4.94E−04	0.71	5.10E−06	1.38
0.00625	1.75E−03	0.40	4.43E−04	0.16	2.07E−06	1.30
Fitted	–	0.75	–	8.80	–	1.55

Fig. 13. The computed solutions of the Carrier–Greenspan problem: Case CG1.

the numerical solutions vary slightly with y, unlike the analytical solution, which is independent of y in this case. In these figures, relatively large errors are found near the wetting front. Comparing these figures, it is observed that spurious oscillations are more forcibly depressed as a smaller value of M is used.

4.3. Drying Riemann problem

In this section, we test the proposed method in a drying situation on a flat bottom. We set up a Riemann problem in which a dry region emerges, shown schematically in Fig. 8. The analytical solution is described in [20]. The configuration shown in Fig. 8 satisfies the drying criterion $\sqrt{gH_l} + \sqrt{gH_r} - u_l + u_r < 0$. Two expansion waves that propagate away from each other result in a dry region, which appears at $t > 0$. The acceleration of gravity is set to 10 m/s^2 and the Courant number is set to 0.1.

The convergence study is conducted with the same sets of parameters used for the dam break problem in the previous section and shown in Table 1. The L^2 errors computed with solutions at 8 s are shown in Tables 5–7. The convergence rates of Case D1 are approximately 1 for ζ and p, and approximately 1.7 for q. These are reasonable convergence rates, considering the fact that this drying Riemann problem also contains a discontinuity in the initial condition. It is also observed that the slope limiter does not significantly affect the order of accuracy of ζ and p. Relatively large degradation occurs in $L^2(q)$ when the slope limiter is applied. It is presumed to be due to the fact that the slope limiter induces a small gradient in the y-direction in the surface elevation and it in turn drives flow in the y-direction.

Shown in Figs. 9–11 are ζ and p computed with $\Delta x = 5$ m. The numerical solutions agree well with the exact solution. The figures
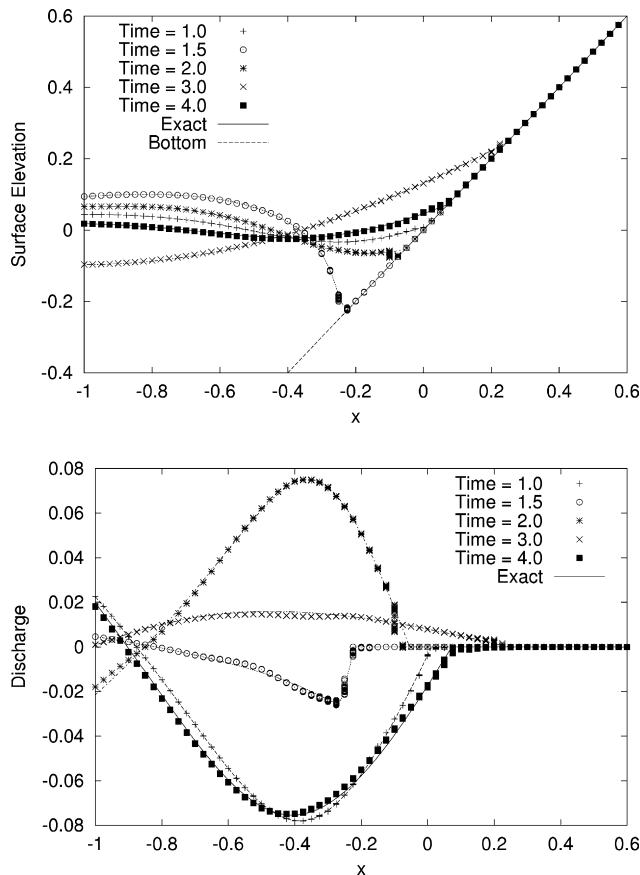
also demonstrate that spurious oscillations are more forcibly depressed as a smaller value of M is used.

4.4. Carrier–Greenspan solution

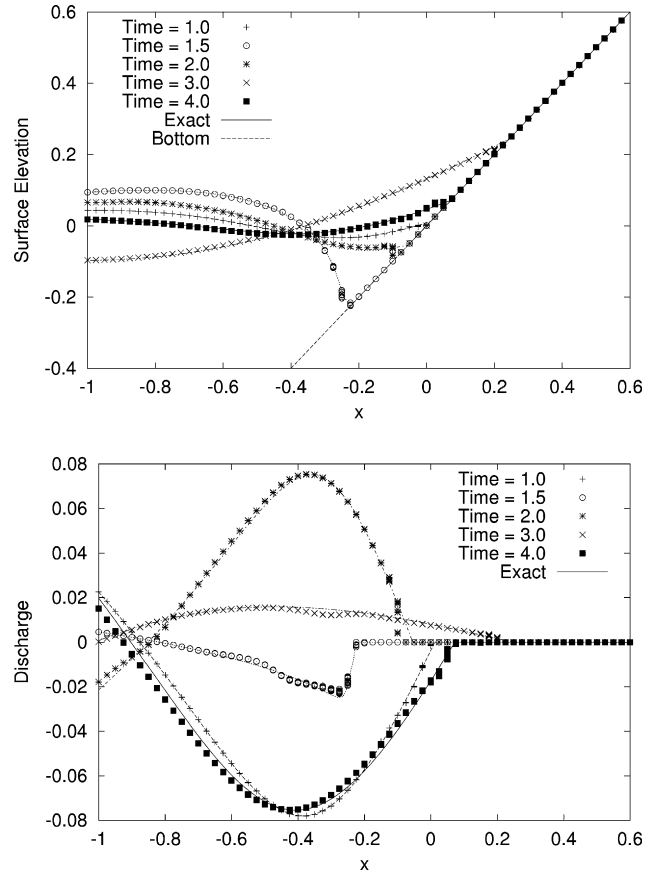The Carrier–Greenspan solution considers a periodic wave propagating up and down a sloping beach [27]. This problem

Fig. 15. The computed solutions of the Carrier–Greenspan problem: Case CG5.

Fig. 14. The computed solutions of the Carrier–Greenspan problem: Case CG3.

Table 14
L^2 error norms and convergence rates of the parabolic bowl problem: $t = \tau/2$.

Δx	$L^2(\zeta)$	Rate	$L^2(p)$	Rate	$L^2(q)$	Rate
400.0	3.56E−06	–	3.05E−06	–	2.54E−06	–
200.0	1.85E−06	0.94	1.39E−06	1.13	1.13E−06	1.17
100.0	9.01E−07	1.04	5.38E−07	1.37	4.49E−07	1.34
50.0	4.10E−07	1.13	2.10E−07	1.36	1.72E−07	1.38
25.0	1.75E−07	1.23	8.00E−08	1.39	6.67E−08	1.37
12.5	7.18E−08	1.29	3.18E−08	1.33	2.69E−08	1.31
Fitted	–	1.13	–	1.33	–	1.33

Table 15
L^2 error norms and convergence rates of the parabolic bowl problem: $t = \tau$.

Δx	$L^2(\zeta)$	Rate	$L^2(p)$	Rate	$L^2(q)$	Rate
400.0	5.48E−06	–	4.99E−06	–	4.66E−06	–
200.0	2.89E−06	0.93	4.43E−06	0.17	3.99E−06	0.22
100.0	1.20E−06	1.27	3.18E−06	0.48	2.77E−06	0.53
50.0	4.96E−07	1.28	1.60E−06	1.00	1.44E−06	0.95
25.0	2.05E−07	1.27	7.09E−07	1.17	6.33E−07	1.18
12.5	8.58E−08	1.26	3.03E−07	1.23	2.73E−07	1.22
Fitted	–	1.22	–	0.83	–	0.84

involves both wetting and drying in each period. We use a configuration similar to that of [20]. The computational domain and a computational mesh with $\Delta x = 0.025$ are shown in Fig. 12. The acceleration of gravity is set to 1 to solve the dimensionless SWE. The Courant number is 0.1. The slope is inclined at 45°. Parameters such as the amplitude and frequency of a periodic wave are selected such that the front reaches infinite steepness against the slope at periodic instants [20]. Unlike two test problems in the previous sections, the solution of this test problem does not contain a discontinuity. The boundary condition along the offshore boundary is applied through the numerical flux.
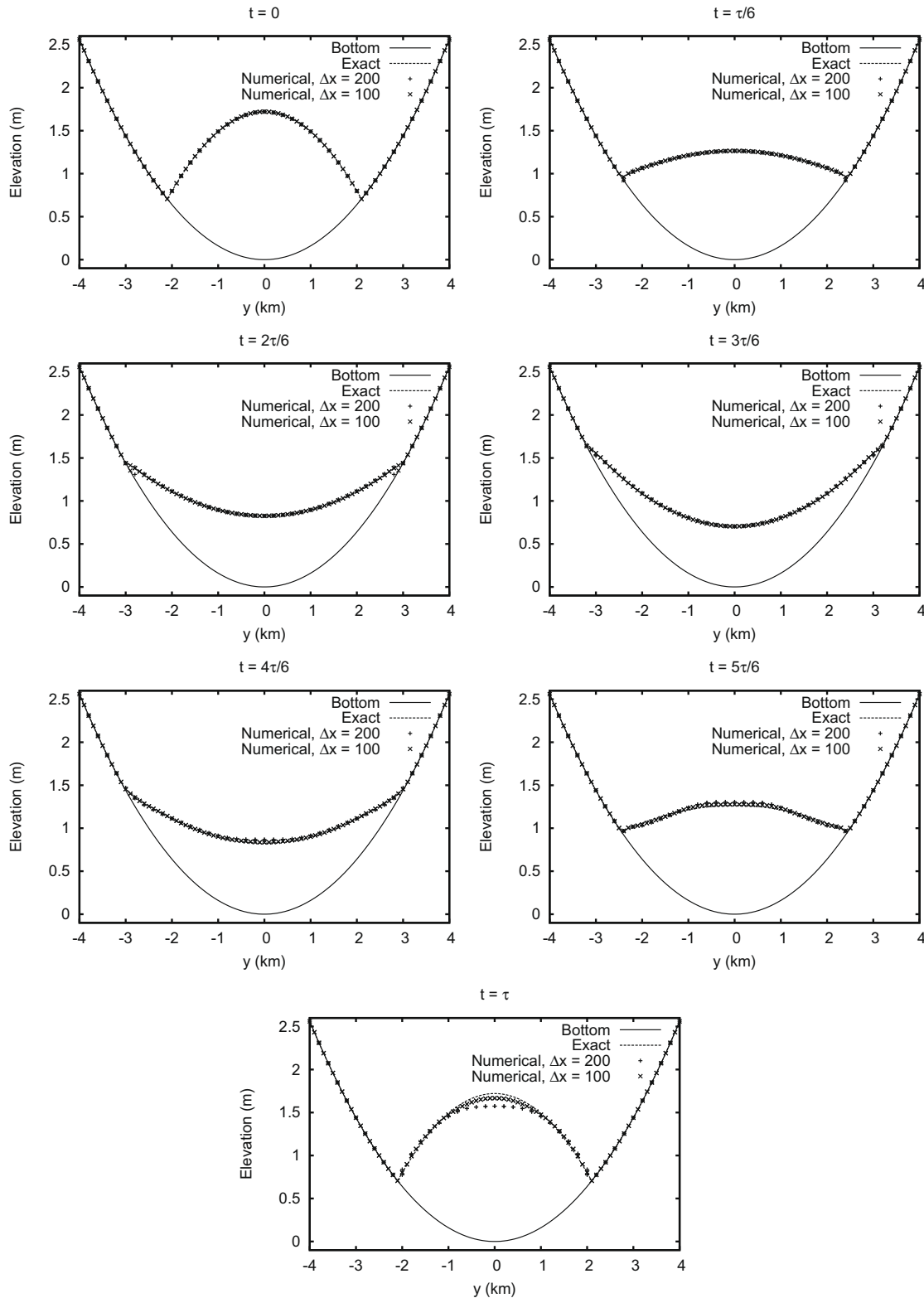

Fig. 16. The initial and computed surface elevations of the parabolic bowl problem.

We compute L^2 error norms for five sets of parameters shown in Table 8. We compare Cases 1, 2 and 3 to find the influence of the slope limiter. We compare Cases 1, 4 and 5 to check the influence of the threshold H_0.

The L^2 errors are computed with solutions at $t = 4$ s and the convergence rates of five cases are shown in Tables 9–13. The computed order of accuracy is approximately 1.1 for ζ and 1.4 for p if no slope limiter is applied and $H_0 = 10^{-5}$. The convergence rate of q is approximately 1.6. The order of accuracy is greater than 1.0 and better than what we obtained in the previous problems with discontinuities. However, it is still less than the optimal order of accuracy, which is 2. This may be attributed to the use of a fixed
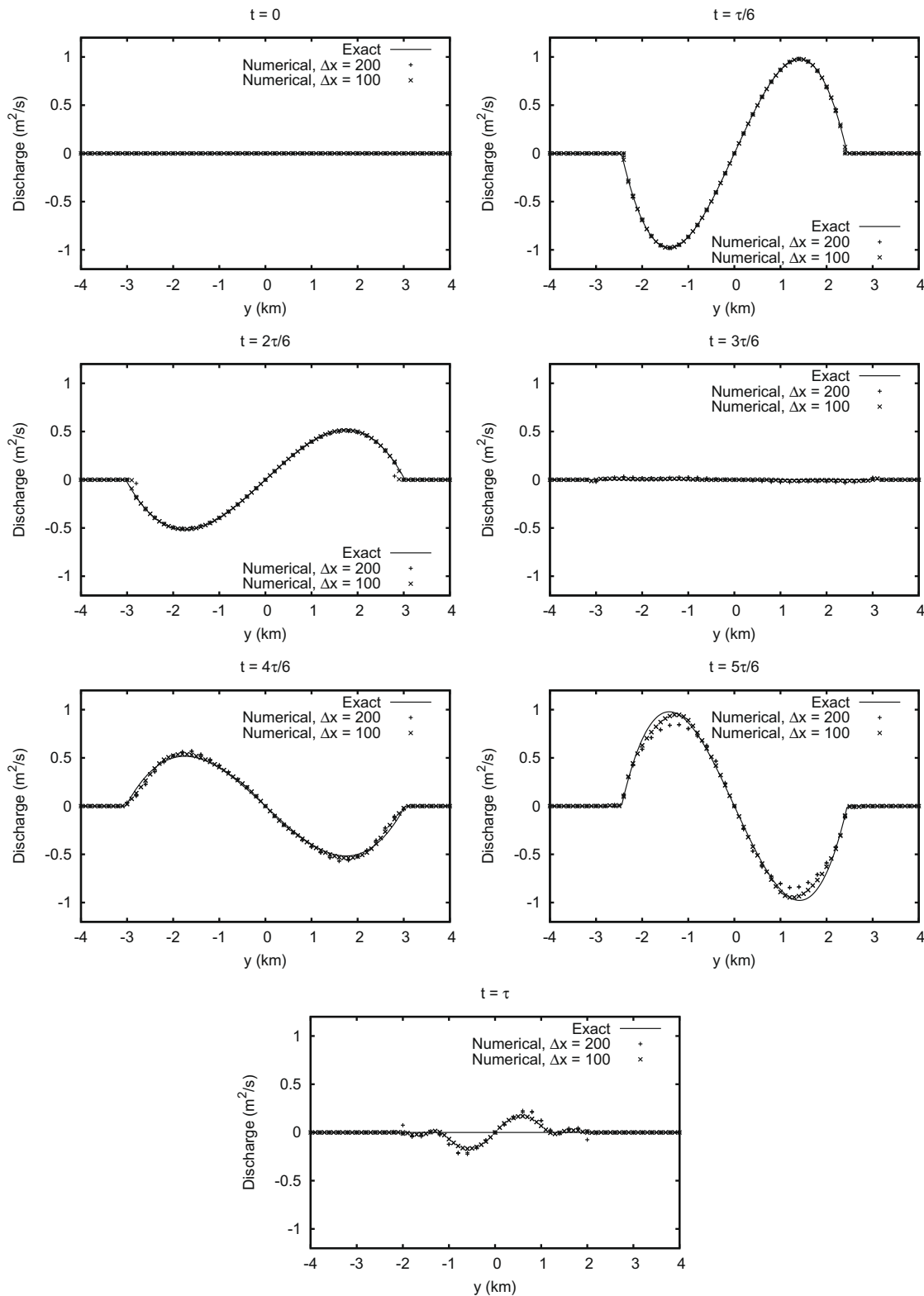

Fig. 17. The initial and computed discharges in the y-direction of the parabolic bowl problem.

mesh, or, as Bokhove discussed in [20], it may be due to the infinite steepness of the surface elevation solution. If we compare Cases CG1, CG2 and CG3, it is confirmed that accuracy is not affected significantly by the slope limiter. Comparing Cases CG1, CG4 and CG5, it is found that the convergence significantly slows down if H_0 is large. It is presumed that the threshold H_0 must approach zero as Δx approaches zero in order to obtain convergence to an exact solution. On the other hand, it is also observed that, in practical applications, accuracy may not be sensitive to a selection of H_0 as long as element sizes are relatively large.

Shown in Figs. 13–15 are the results of Cases CG1, CG3 and CG5, respectively. All the results agree well with the exact solution. A steep gradient in the solution at $t = 1.5$ is also captured well.

4.5. Parabolic bowl

Here we test the proposed method for a two-dimensional axi-symmetric phenomena. The bottom depth is a paraboloid and prescribed as $h(x,y) = \alpha r^2$ where α is a positive constant and $r = \sqrt{x^2 + y^2}$. At an initial state, the water surface is also in a parabolic shape and the velocity is zero. The exact solution is periodic in time with a period τ. One can find the exact solution in [28]. The water depth $H(r,t)$ is non-zero for $r < \sqrt{(X + Y\cos\omega t)/\alpha(X^2 - Y^2)}$ and the exact solution is given within the range as follows:

$$H(r,t) = \frac{1}{X + Y\cos\omega t} + \alpha(Y^2 - X^2)\frac{r^2}{(X + Y\cos\omega t)^2}, \quad (42)$$

$$(u(x,y,t), v(x,y,t)) = -\frac{Y\omega\sin\omega t}{X + Y\cos\omega t}\left(\frac{x}{2}, \frac{y}{2}\right), \quad (43)$$

where $\omega^2 = 8g\alpha$ and X and Y are constants such that $X > 0$ and $|Y| < X$. The period is $\tau = 2\pi/\omega$.

We use a similar set of parameters to what Ern et al. used in [21]. The constants, α, X and Y are set to 1.6×10^{-7} m^{-1}, 1 m^{-1}, and -0.41884 m^{-1}, respectively. The acceleration of gravity is set to 10 m^2/s. The computational domain is a square with the side length of 8000 m. The Courant number is set to 0.12. The slope limiter is applied with $M = 0.01$.

We compute the L^2 error norms for five different mesh resolutions. The errors are computed at two times: $t = \tau/2$ and $t = \tau$. Since the exact solution is periodic and wetting occurs in the first half of a period and drying occurs in the second half of a period, the norms measured at $t = \tau/2$ and $t = \tau$ represent errors in wetting and drying, respectively. The obtained error norms and orders of convergence are shown in Tables 14 and 15.

The computed convergence rate is 1.1 for ζ and is 1.3 for p and q in the wetting stage (Table 14). The computed convergence rates in the drying stage are 1.2 for ζ and 0.8 for p and q. These rates are below the optimal value, which is 2, but are acceptably good for the reasons stated in the previous section. The errors and convergence rates for ζ in the wetting and drying stages are comparable while the errors in p and q in the drying stage are larger by an order of magnitude than those in the wetting stage if compared at $\Delta x = 12.5$ m. Also, the convergence rates for p and q in the drying stage starts small, but increase steadily as the grid resolution gets improved. This indicates that numerical solutions of p and q enter an asymptotic range later than ζ. If we compare the convergence rates at $\Delta x = 12.5$ m, they are comparable in the wetting and drying stages. Overall, one may get a worse accuracy in p and q in the drying stage, but one can expect accuracy improvement both in the wetting and drying stages at rates greater than 1 in all dependent variables, ζ, p and q once a resolution reaches an asymptotic range.

Plotted in Figs. 16 and 17 are ζ and q along $x = 0$, respectively. Exact solutions and numerical solutions obtained with two grid spacings, $\Delta x = 100$ and 200 m, are compared in the figures. One may notice that more errors are found in the drying stage ($\tau/2 < t < \tau$). This may indicate that our wetting and drying treatment can be improved further especially in the drying stage.

5. Conclusions

A wetting and drying treatment was proposed for the RKDG discretization to the shallow water equations. The proposed method uses fixed meshes. A post-process operator, which is called the PD operator, was introduced as a part of the proposed wetting and drying treatment. A combination of the proposed wetting and drying treatment and a TVB slope limiter was tested. It was observed that our wetting drying treatment and the tested slope limiter work fine if they are applied exclusively in each element.

The order of convergence was examined for four test problems. The numerically estimated order of accuracy reaches 1 for solutions with discontinuities and it becomes considerably better than 1, but less than the optimal rate, which is 2, for smooth solutions.

The numerical flux is controlled in such a way that the positivity of the mean water level within each finite element is ensured with any time step as long as the CFL condition is not violated. This special flux treatment on the numerical flux enabled us to compute all the test cases stably with reasonably large Courant numbers. No excessive drying was detected in any element during the computations and therefore there was no need to add mass to such elements. Without this flux treatment, one may need to either use much smaller time step or add mass to excessively dry elements.

The proposed method was tested only with the linear triangular element. Extention to higher order interpolation is open to future work.

Acknowledgements

References

[1] D.R. Lynch, W.G. Gray, A wave equation model for finite element tidal computations, Comput. Fluids 7 (1979) 207–228.
[2] H. Ma, A spectral element basin model for the shallow water equations, J. Comput. Phys. 109 (1993) 133–149.
[3] M. Iskandarani, D.B. Haidvogel, John P. Boyd, A staggered spectral element model with application to the oceanic shallow water equations, Int. J. Numer. Methods Fluids 20 (1995) 393–414.
[4] K. Kashiyama, H. Ito, M. Behr, T. Tezduyar, Three-step explicit finite element computation of shallow water flow on massively parallel computer, Int. J. Numer. Methods Fluids 21 (1995) 885–900.
[5] J. Matsumoto, T. Umetsu, M. Kawahara, Stabilized bubble function method for shallow water long wave equation, Int. J. Comput. Fluid Dyn. 17 (2003) 319–325.
[6] J.J. Westerink, J.C. Feyen, J.H. Atkinson, R.A. Luettich, C. Dawson, H.J. Roberts, M.D. Powell, J.P. Dunion, E.J. Kubatko, H. Pourtaheri, A basin to channel scale unstructured grid hurricane storm surge model applied to Southern Louisiana, Mon. Weather Rev. 136 (2008) 833–864.
[7] D. Schwanenberg, J. Kongeter, A discontinuous Galerkin method for the shallow water equations with source terms, in: B. Cockburn, G.E. Karniadakis, C.W. Shu (Eds.), Discontinuous Galerkin Methods, Springer, 2000, pp. 419–424.
[8] H. Li, R. Liu, The discontinuous Galerkin finite element method for the 2D shallow water equations, Math. Comput. Simul. 56 (2001) 223–233.
[9] V. Aizinger, C. Dawson, A discontinuous Galerkin method for two-dimensional flow and transport in shallow water, Adv. Water Resour. 25 (2002) 67–84.
[10] D. Schwanenberg, M. Harms, Discontinuous Galerkin finite-element method for transcritical two-dimensional shallow water flows, J. Hydraul. Engrg. 130 (2004) 412–421.
[11] S. Fagherazzi, P. Rasetarinera, M.Y. Hussaini, D.J. Furbish, Numerical solutions of the dam-break problem with a discontinuous Galerkin method, J. Hydraul. Engrg. 130 (2004) 532–539.

[12] C. Eskilsson, S.J. Sherwin, A triangular spectral/hp discontinuous Galerkin method for modelling 2D shallow water equations, Int. J. Numer. Methods Fluids 45 (2004) 605–623.
[13] J.-F. Remacle, S.S. Frazão, X. Li, M.S. Shephard, An adaptive discretization of shallow-water equations based on discontinuous Galerkin methods, Int. J. Numer. Methods Fluids 52 (2006) 903–923.
[14] F.X. Giraldo, T. Warburton, A high-order triangular discontinuous Galerkin oceanic shallow water model, Int. J. Numer. Methods Fluids 56 (2008) 899–925.
[15] C. Dawson, J.J. Westerink, J.C. Feyen, D. Pothina, Continuous, discontinuous and coupled discontinuous–continuous Galerkin finite element methods for the shallow water equations, Int. J. Numer. Methods Fluids 52 (2006) 63–88.
[16] E.J. Kubatko, J.J. Westerink, C. Dawson, hp discontinuous Galerkin methods for advection dominated problems in shallow water flow, Comput. Methods Appl. Mech. Engrg. 196 (2006) 437–451.
[17] C. Nielsen, C. Apelt, Parameters affecting the performance of wetting and drying in a two-dimensional finite element long wave hydrodynamic model, J. Hydraul. Engrg. 129 (2003) 628–636.
[18] P.D. Bates, J.-M. Hervouet, A new method for moving-boundary hydrodynamic problems in shallow water, in: Proceedings of Mathematical, Physical and Engineering Sciences vol. 455, 1999, pp. 3107–3128.
[19] S.F. Bradford, B.F. Sanders, Finite-volume model for shallow-water flooding of arbitrary topography, J. Hydraul. Engrg. 128 (2002) 289–298.
[20] O. Bokhove, Flooding and drying in discontinuous Galerkin finite-element discretizations of shallow-water equations. Part 1: one dimension, J. Sci. Comput. 22–23 (2005) 47–82.
[21] A. Ern, S. Piperno, K. Djadel, A well-balanced Runge–Kutta discontinuous Galerkin method for the shallow-water equations with flooding and drying, Int. J. Numer. Methods Fluids 58 (2008) 1–25.
[22] B. Cockburn, C.W. Shu, The Runge–Kutta discontinuous Galerkin method for conservation laws V: multidimensional systems, J. Comput. Phys. 141 (1998) 199–224.
[23] M. Dubiner, Spectral methods on triangles and other domains, J. Sci. Comput. 6 (1991) 345–390.
[24] E.J. Kubatko, J.J. Westerink, C. Dawson, Semi discrete Galerkin methods and stage-exceeding-order strong-stability-preserving Runge–Kutta time discretizations, J. Comput. Phys. 222 (2007) 832–848.
[25] S. Gottlieb, C.W. Shu, E. Tadmor, Strong stability-preserving high-order time discretization methods, SIAM Rev. 43 (2001) 89–112.
[26] J.J. Stoker, Water Waves, John Wiley Sons, 1958. p. 312.
[27] G.F. Carrier, H.P. Greenspan, Water waves of finite amplitude on a sloping beach, J. Fluid Mech. 4 (1958) 97–109.
[28] W.C. Thacker, Some exact solutions to the nonlinear shallow-water wave equations, J. Fluid Mech. 107 (1981) 499–508.